ADVANCED FUNCTIONAL MATERIALS
www.afm-journal.de

Check for updates

Epitaxial Growth of 1D Atomic Chain Based Se Nanoplates on Monolayer ReS_2 for High-Performance Photodetectors

Jing-Kai Qin, Gang Qiu, Wen He, Jie Jian, Meng-Wei Si, Yu-Qin Duan, Adam Charnas, Dmitry Y. Zemlyanov, Hai-Yan Wang, Wen-Zhu Shao, Liang Zhen, Cheng-Yan Xu, and Peide D. Ye**

Mixed-dimensional (0D, 1D, and 3D) heterostructures based on 2D layered materials have been proven as a promising candidate for future nanoelectronics and optoelectronics applications. In this work, it is demonstrated that 1D atomic chain based Se nanoplates (NPs) can be epitaxially grown on monolayer ReS_2 by a chemical transport reaction, thereby creating an interesting mixed-dimensional Se/ReS_2 heterostructure. A unique epitaxial relationship is observed with the (110) planes of the Se NPs parallel to the corresponding ReS_2 (010) planes. Experimental and theoretical studies reveal that the Se NPs could conjugate with underlying monolayer ReS_2 via strong chemical hybridization at heterointerface, which is expected to originate from the intrinsic defects of ReS_2. Remarkably, photodetectors based on Se/ReS_2 heterostructures exhibit ultrahigh detectivity of up to 8×10^{12} Jones, and also show a fast response time of less than 10 ms. These results illustrate the great advantage of directly integrated 1D Se based nanostructure on planar semiconducting ReS_2 films for optoelectronic applications. It opens up a feasible way to obtain mixed-dimensional heterostructures with atomic interfacial contact by epitaxial growth.

1. Introduction

Recently, 2D + nD ($n = 0$, 1, and 3) mixed-dimensional heterostructures have been intensively investigated for their potential applications in modern nanoelectronics and optoelectronics.[1–9] Most of these heterostructures are formed by a top-down approach with a polymethyl methacrylate (PMMA)-assisted transfer process,[10,11] which makes it possible to integrate variety of materials with different functionalities. However, the manual transfer technique provides too much indeterminacy to control the stacking orientation and contact quality between materials. On the other hand, the bottom-up approach, that is, direct epitaxial growth by a chemical vapor deposition (CVD) process, provides a powerful approach to fabricate heterostructures with particular stacking modes. A variety of hybrid structures have already been constructed using this strategy, including MoS_2/WS_2, $MoSe_2$/graphene, MoS_2/SnS_2, and CdS/MoS_2.[8,12–14] However, it remains a challenge to control the interfacial quality, since the dissimilar materials in such heterostructure are stacked together by van der Waals (vdW) interaction without covalent bonding. The vdW gap could still significantly deteriorate the charge transfer efficiency and affect the physical properties of the heterostructure.[15–18]

Most of the components in the reported mixed-dimensional heterostructures are layered materials with the same planar crystal structures. However, 1D van der Waals elemental materials Se and Te could also exhibit interesting physical properties such as high photoconductivity, high piezoelectricity, thermoelectricity, and nonlinear optical responses.[19–24] In trigonal Se, the Se atoms are covalently bonded along the c axis into a spiral chain, and these isolated chains could be stacked radially by weak van der Waals interactions to form a hexagonal structure. The direct growth of such 1D van der Walls materials on 2D layers is unexplored and these heterostructures could also be of great interest for applications. However, lattice mismatch creates huge challenges to directly integrate 1D Se/Te into other planar 2D materials. Different from commonly studied group II–IV transition metal dichalcogenides (TMDs) with triangular prismatic crystal structures (such as MoS_2 and WSe_2), the ReS_2 lattice is highly asymmetric due to Peierls distortion. The unique 1T' structure introduces many distinct binding sites for atom absorption on the ReS_2 surface, resulting in the spontaneous growth in vertical mode.[25–27] Inspired by this fact, we postulate that these sites with high chemical activity could facilitate the subsequent heterogeneous growth by covalent bonding. Thus, we could design and prepare ReS_2-based intimate heterostructures with ideal interfacial quality.

J.-K. Qin, G. Qiu, Dr. M.-W. Si, Y.-Q. Duan, A. Charnas, Prof. D. Y. Zemlyanov, Prof. P. D. Ye
School of Electrical and Computer Engineering
Purdue University
West Lafayette, IN 47907, USA
E-mail: yep@purdue.edu

J.-K. Qin, W. He, Prof. W.-Z. Shao, Prof. L. Zhen, Prof. C.-Y. Xu
School of Materials Science and Engineering
Harbin Institute of Technology
Harbin 150001, P. R. China
E-mail: cy_xu@hit.edu.cn

Dr. J. Jian, Prof. H.-Y. Wang
School of Materials Science and Engineering
Purdue University
West Lafayette, IN 47907, USA

DOI: 10.1002/adfm.201806254

© 2018 WILEY-VCH Verlag GmbH & Co. KGaA, Weinheim

In this work, we demonstrate that 1D van der Waals Se formed as nanoplates (NPs) can directly grow on monolayer ReS_2, thereby creating an interesting mixed-dimensional Se/ReS_2 heterostructure. This heterogeneous growth exhibits an epitaxial relationship with the (110) planes of the Se lattice parallel to the (010) planes of ReS_2. Detailed atomic force microscopy (AFM) and X-ray photoelectron spectroscopy (XPS) characteristics reveal an atomically close contact between Se and ReS_2 with covalent bonding, which is further confirmed by density functional theory (DFT) calculations. Photodetectors based on the Se/ReS_2 heterostructure present ultrahigh detectivity of 8×10^{12} Jones and a fast response time of less than 10 ms, significantly superior to the performance of photodetectors based on other analogue hybrid structures. This work provides us a new angle to design and prepare mixed-dimensional heterostructures based on 2D materials, and it also opens up a useful platform of novel nanomaterials systems for nanoscale electronics and optoelectronics applications.

2. Results and Discussion

Figure 1a shows a schematic illustration of the epitaxially grown Se/ReS_2 heterostructures, which are prepared by a two-step vapor deposition process as illustrated in Figure S1 (Supporting Information). In the first stage, ReS_2 monolayers are synthesized on a freshly cleaved fluorophlogopite mica substrate by CVD in a tube furnace, where ReO_3 powders react with sulfur vapor at a high temperature of 600 °C for 10 min. The subsequent Se/ReS_2 heterogeneous growth was conducted using vacuum vapor deposition at 275 °C. The mica substrate coated with ReS_2 monolayers is placed at the end of a quartz ampoule with Se powder in the center, and it is then placed in a furnace and vacuum pumped until the pressure is less than 10^{-4} Torr. After 30 min of reaction, trigonal Se NPs are observed on the monolayer ReS_2 surface (Figure 1b).

The Se/ReS_2 heterostructures were characterized by scanning electron microscopy (SEM) as shown in Figure 1c and Figure S2 (Supporting Information). Most of the Se NPs exhibit triangular or hexagonal shapes with lateral lengths ranging from 100 to 800 nm. Figure 1d shows a cross section of the Se-ReS_2 heterostructures. It is clear that all the Se NPs have similar heights with maximum value less than 100 nm, which is consistent with the AFM characterization (Figure 1e and Figure S3, Supporting Information). It is worth noting that the rate of nucleation of Se NPs at the edge area is much higher than that in the center, as illustrated in Figure 1e. In CVD-grown 2D monolayers, the edge area of the flakes is expected to have large number of structural imperfections,[28] and these imperfections with high electron affinity could act as active nucleation centers for the subsequent Se epitaxial growth. The monolayer ReS_2 becomes fully covered by thick planar Se crystals as the growth time is extended to 1 h (Figure S4, Supporting Information). The Se crystallization exhibits strong selectivity toward the ReS_2 growth template. As shown in Figure S5 (Supporting Information), Se tends to grow into long 1D nanobelts (Se NBs) in the ReS_2-free area on mica, which are totally different from the triangular or hexagonal nanoplates grown on monolayer ReS_2 under the same condition.

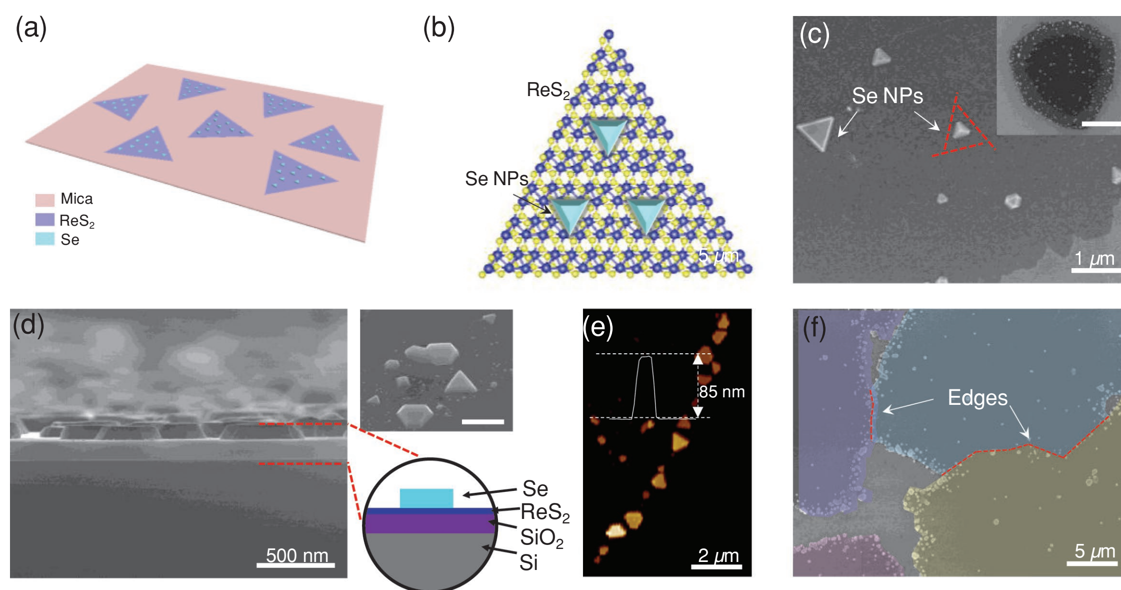

Figure 1. Characterization of epitaxial growth of Se NPs on ReS_2 monolayers. a) Model of the Se/ReS_2 heterostructures grown on the mica substrate, where Se NPs are located on the triangular monolayer ReS_2. b) Schematic illustration of the Se/ReS_2 heterostructure. c) SEM image at the edge area of the flake, showing the triangular and hexagonal shapes of Se NPs. Inset image shows a top-view of ReS_2 monolayer with Se NPs, scale bar is 5 µm. d) Cross-section SEM image of Se NPs grown on ReS_2 monolayer after being transferred onto SiO_2/Si substrate. Inset is a 45°-titled view, scale bar is 1 µm. e) AFM height profile of Se NPs. f) Top view SEM image showing four adjacent ReS_2 domains, all the Se NPs tend to grow around edge area. Each individual ReS_2 domain is marked with a different color.

© 2018 WILEY-VCH Verlag GmbH & Co. KGaA, Weinheim

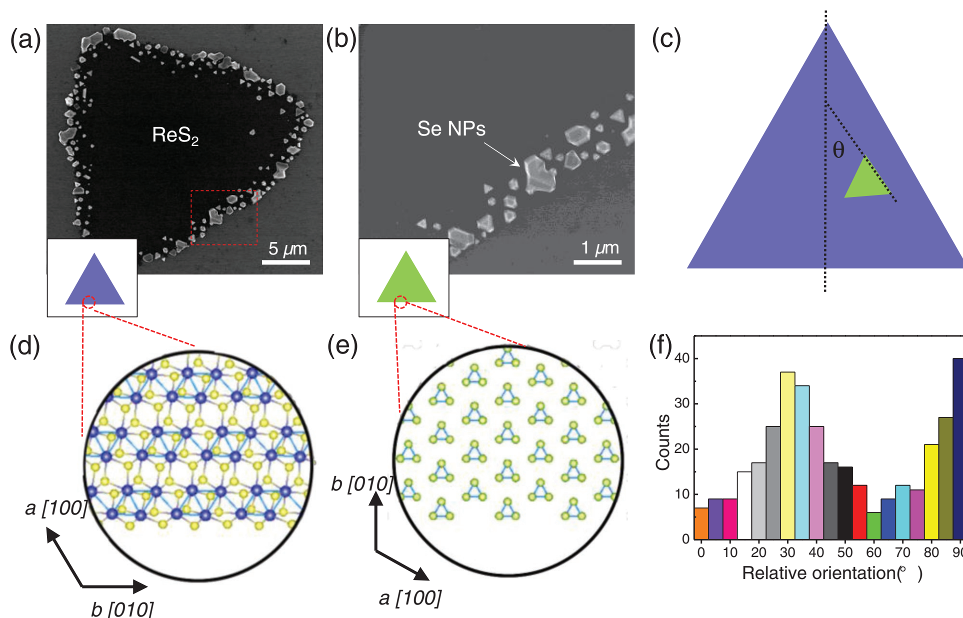

Figure 2. The epitaxy relationship between Se NPs and ReS_2 monolayer. a) SEM images of Se NPs on a triangular ReS_2 monolayer. b) Enlarged SEM image of the edge area. c) Schematics of the epitaxy relationship between Se NPs and ReS_2. d,e) Schematics of the crystal structure of ReS_2 sheet and Se NPs at the edge area. f) Statistical diagram of the relative angle between the edges of NPs and ReS_2.

To determine the epitaxy relationship between Se NPs and ReS_2, orientation information collected from SEM images are statistically analyzed. **Figure 2**a shows the top-view SEM image of the Se NPs on an individual monolayer ReS_2. It should be noted that these triangular-shaped ReS_2 monolayers are expected to grow with the Re chains' *b* [010] direction parallel with the edge (Figure 2d), which is confirmed by high-resolution transmission electron microscopy (HRTEM) discussed later. Thus, it would be straightforward to determine the crystalline direction of the Se NPs by comparing them to the edge of the ReS_2 flakes (Figure 2b,e). The statistics chart reveals that the Se NPs have a tendency to grow with the triangle sides parallel to the *b* [010] direction of ReS_2 (Figure 1e,f).

We transferred these Se/ReS_2 heterostructures onto Cu grids and performed transmission electron microscopy (TEM) to further identify the morphology and epitaxy relationship of the heterostructures. Triangular or hexagonal Se NPs can be clearly seen as shown in **Figure 3**a,b. High-angle annular dark field scanning-transmission electron microscope (STEM) (HAADF-STEM) was performed on a pure ReS_2 monolayer area (Figure 3c). Distinct Re–Re DS-chains could be observed, and the fringe space of (010) lattice planes was measured to be 3.4 Å, well in agreement with the optimized ReS_2 lattice constant. The STEM image obtained of Se NPs reveals a perfect hexagonal crystal structure, which indicates that the Se NPs are grown with the [001] axis vertically aligned with underlying ReS_2 (Figure 3d). To further identify the exact epitaxy relationship, selected area electron diffraction (SAED) patterns were also extracted (Figure 3e). Two sets of sixfold symmetric diffraction spots could be clearly identified, where the brighter and outer set corresponds to the Se NPs while the weaker one belongs to the monolayer ReS_2. By comparing the SAED pattern with the morphology, we can conclude that the Se NPs are epitaxially grown with the (110) plane parallel to the (010) plane of ReS_2 (Figure 3f).

The quality of interface contact is another important issue that must be addressed. It is necessary to determine the contact mode of Se/ReS_2 heterostructure, since high-quality contact would better facilitate charge transfer and separation at interface.[29,30] As shown in **Figure 4**a, the Se NPs were scratched away using AFM, and the contact quality could be directly evaluated by the ratio of lift-off area to the underlying ReS_2. Figure 4b,c shows typical SEM images of the Se/ReS_2 heterostructure before and after the Se NPs are scratched away. We can see that the underlying ReS_2 was completely lifted off, exposing the bare mica substrate with the triangular shape. The corresponding AFM height profile was presented in Figure 4d. The pit depth is about 1.0 nm, almost the same as the thickness of monolayer ReS_2, and no ReS_2 residues could be detected in the exposed area. The EDX elemental maps of the scratched Se NPs are presented in Figure S6 (Supporting Information), where Re and S could be distinctly detected on the bottom of Se NPs. The results indicate that the monolayer ReS_2 is conjoined tightly with above Se NPs by the whole contact area with high interface quality.

The Se/ReS_2 heterostructure is characterized by Raman spectroscopy with a 532 nm laser at room temperature (Figure 4e,f). The peak located at ≈233 cm^{-1} can be distinctly detected, which belongs to the E^2 mode of trigonal Se.[20,31] All peaks related to ReS_2 exhibit a clear blue shift, with a maximum difference of up to 3.3 cm^{-1} for the III peak of ReS_2 (≈238 cm^{-1}). In order to evaluate the influence of the hetero-interface on the Raman shift in ReS_2, we have constructed a Se NB-ReS_2 heterostructure by PMMA-assisted transfer technique (Figure S7, Supporting Information), where the Se NBs and underlying ReS_2 are expected to contact with each other by van der Waals interaction without chemical hybridization. Remarkably, in such kind of hybrid structure, the Raman peaks belonging to ReS_2 do not show any change compared with pure

© 2018 WILEY-VCH Verlag GmbH & Co. KGaA, Weinheim

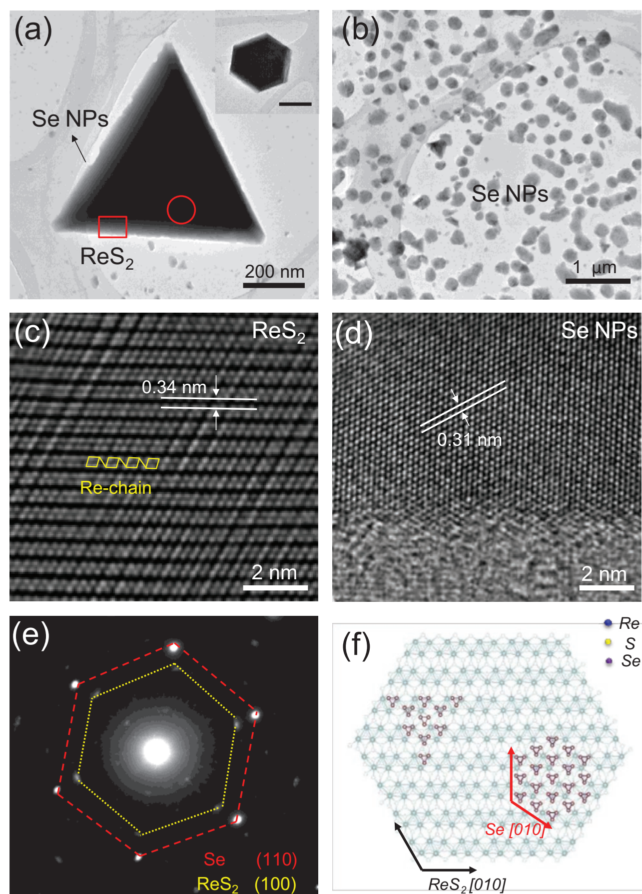

Figure 3. TEM characterization of Se/ReS_2 heterostructure. a,b) Low-magnification TEM images of triangular Se NPs. Inset shows the hexagonal Se NPs, scale bar is 500 nm. c,d) STEM image of pure ReS_2 monolayer marked with red rectangle and Se NPs marked with red circle in (a). e) Selected area electron diffraction (SAED) of heterostructures. f) Schematic model of the Se/ReS_2 heterostructures.

monolayer ReS_2, indicating that the shift of Raman peaks in ReS_2 is mainly determined by the chemically hybridized Se NPs at the interface. In the Se NP-ReS_2 heterostructure, electrons in ReS_2 tend to transfer from Se due to the difference of Fermi levels in band alignment,[32,33] and the Se-Re covalent bond at interface acts as a fast transmission path for charge transfer.[7] The reduction of electron density in ReS_2 would result in the weakening of the electron-phonon coupling effect and explains the observed Raman peak shift.[34] XPS was also performed to investigate the influence of interface hybridization on the electronic structure of Se-ReS_2 heterostructure (Figure S8, Supporting Information). Remarkably, the binding energy of Se 3d peaks for Se NPs-ReS_2 nanohybrids slightly decreases by 0.4 eV compared with Se NBs-ReS_2 heterostructure, while the Re 4f peaks shift by 0.8 eV toward higher binding energy. This result further confirms the existence of the Se-Re covalent bonds and the efficient charge transfer at the chemically hybridized Se NP-ReS_2 heterointerface.[35,36]

Epitaxial growth only happens when two materials have the same lattice constant in a particular orientation.[37,38] Trigonal Se has the perfect hexagonal crystal structure with in-plane spacing of 0.378 nm along the [100] direction, while ReS_2 exhibits a distorted 1T' hexagonal structure with 0.654 nm for *a* axis and 0.635 nm for *b* axis,[39,40] as shown in Figure S9 (Supporting Information). The lattice mismatch is far too large to be accommodated by coherent strain. However, a good coincidence of the lattice parameters would be realized by aligning the [$\bar{1}$10] direction (≈0.646 nm) of Se to the [100] direction (≈0.635 nm) of ReS_2. The residual mismatch associated with this combination is only ≈1.5%, which is small enough for strain accommodation. Indeed, being very different from commonly studied group II–VI TMDs such as MoS_2 and WSe_2, which possess trigonal prismatic crystal structures, the distorted 1T' structure would lead to an inherent asymmetry with Peierls distortion in ReS_2. The adjacent 4 Re atoms would be pinched together to form a super lattice structure of Re chains, which would introduce many distinct binding sites for Re absorption (**Figure 5**a and Figure S10, Supporting Information). Among them, Re atoms are most likely to be absorbed on site B due to the lower forming energy, and they could bind with three neighboring Re atoms, resulting in the dislocation of the nearby S atoms (Figure 5b). In the following Se epitaxial growth process, these protruding Re atoms in such an under-coordinated crystal configuration could easily interact with Se atoms and act as nucleating seeds for Se NP growth (Figure 5c). Finally, trigonal Se could grow along the out-of-plane direction into 1D chains and form a stable Se/ReS_2 heterojunction (Figure 5d,e).

To evaluate the doping effect of Se NPs on monolayer ReS_2, we fabricated field effect transistors through a standard electron beam lithography (EBL) process (Figure S11, Supporting Information). Compared with pure monolayer ReS_2 devices, the hybrid devices exhibit a smaller on/off ratio (≈10^4), and the on-state current is reduced by one order of magnitude at the same source-drain voltage (Figure S12, Supporting Information). The field-effect mobility (μ) can be extracted from the transfer curves using $\mu = L_{in}/W \times (1/C_{bg}) \times dI/dV_{bg}$, where L_{in} and W represent the channel length and width, respectively, and C_{bg} is the capacitance of SiO_2. The value is expected to be 22 $cm^2\ V^{-1}\ s^{-1}$ at 300 K for a monolayer ReS_2 device. After Se epitaxy growth, the mobility is reduced significantly to 0.17 $cm^2\ V^{-1}\ s^{-1}$ mainly due to the reduction of the drain current induced by the p-type Se NPs. In order to better understand the change in transport behavior, we have used DFT calculations to obtain the electronic band structure of the Se/ReS_2 hybrid system. As shown in Figure 5f,g, after Se growth, some deep-impurity levels are introduced around the Fermi level, which would lead to the accumulation of electrons at negative back gate voltages and a high level of off-state current.[41] On the other hand, the p-type Se NPs could also act as electron acceptors and reduce the carrier density in underlying ReS_2. Thus, the on-state current could be greatly suppressed, resulting in the low on-off ratio observed in the Se/ReS_2 hybrid devices.[42]

We have systematically investigated the optoelectronic properties of Se/ReS_2 based photodetectors. A device schematic is illustrated in **Figure 6**a. Figure 6b shows typical output characteristics ($I_{ds} - V_d$) of hybrid devices under different laser illumination conditions (λ = 322, 370, 417, 532, and 633 nm), where the incident power was fixed at 0.24 mW cm^{-2}. The photocurrent rises gradually with the decrease of laser wavelength,

© 2018 WILEY-VCH Verlag GmbH & Co. KGaA, Weinheim

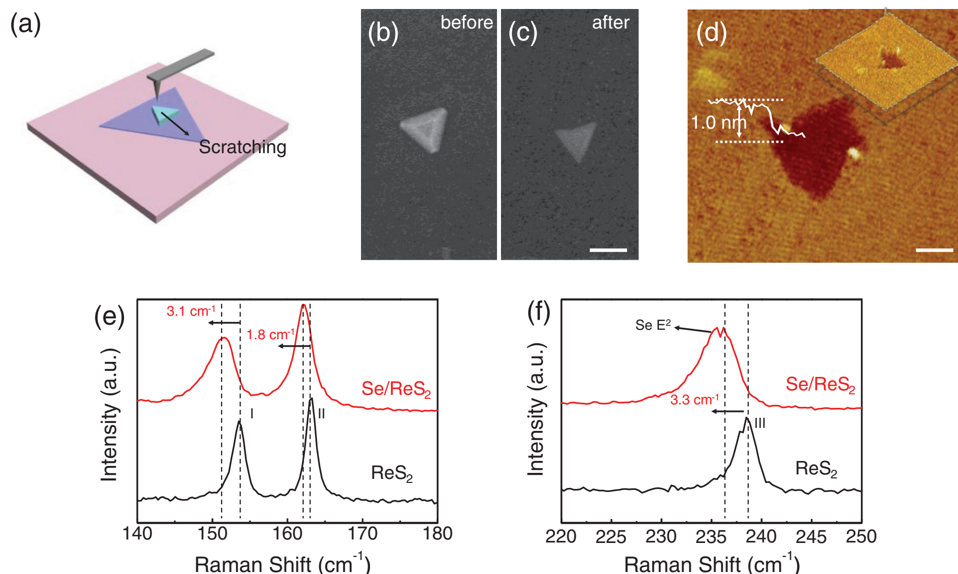

Figure 4. Contact evaluation of the interface between Se NPs and ReS_2 monolayer. a) Schematics of AFM stretching test. b,c) STM image of Se/ReS_2 heterostructure before and after Se NPs scratched away. The scale bar is 1 µm. d) Corresponding AFM height profile of pits on ReS_2 monolayers. Inset shows a 3D view. The scale bar is 500 nm. e,f) Comparison of Raman spectra of Se/ReS_2 heterostructure and pure ReS_2 monolayer.

which can be attributed to the increasing photogenerated electron-hole pairs by higher photon energies.[43] As an important figure-of-merit for photodetector, the dark current of Se/ReS_2 hybrid device was measured to be less than 10 pA at $V_g = -30$ V (Figure 6c), much lower than that in monolayer ReS_2 devices (≈5 nA). Two important parameters for photodetectors, photoresponsivity (R_λ) and detectivity (D^*), are defined as

$$R_\lambda = I_{ph}/PS \quad (1)$$

$$D^* = RS^{1/2}/(2qI_d)^{1/2} \quad (2)$$

where I_{ph}, I_d, P, and S represent the photocurrent, dark current, incident power, and effective illuminated area, respectively.

The maximum R_λ was estimated to be 36 A W^{-1} with a 0.03 mW cm^{-2} incident power density ($V_{ds} = 3$ V and $V_g = 0$ V). This value is comparable with previously reported photodetectors based on mixed-dimensional heterostructures such as CdS-MoS_2 and $WS_2/CH_3NH_3PbI_3$.[5,8,42–45] Under illumination, most of the photoexcited electrons in ReS_2 are trapped in the conduction band due to a high energy barrier (Figure S13, Supporting Information), which is introduced by the difference in conduction levels . At the same time, photogenerated electrons in Se NPs could quickly transfer to underlying ReS_2, whereas holes are confined in the Se NPs. Both the interstructure absorption in ReS_2 and carrier transfer from Se could contribute to the channel current under illumination, leading to the enhancement of responsivity in the Se-ReS_2

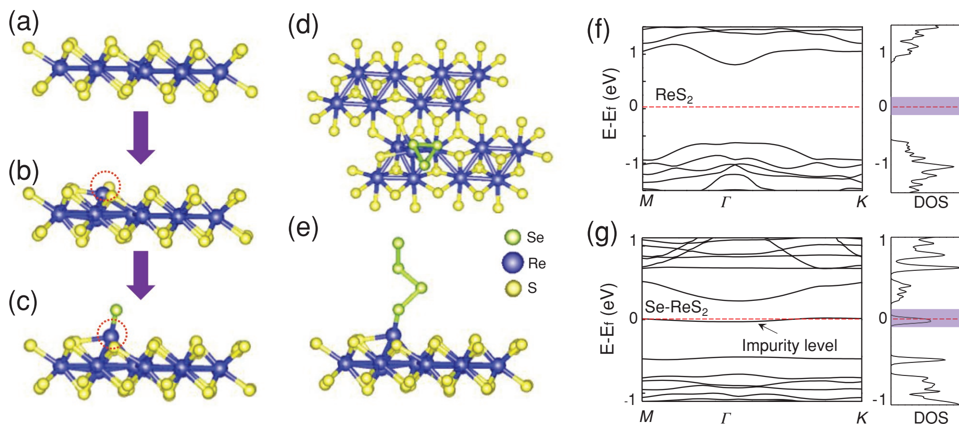

Figure 5. The growth mechanism of Se NPs on ReS_2 simulated by first-principles calculation. a) Structure model showing the pristine ReS_2 super cell. b) A protruding Re atom absorbed on ReS_2 surface, which could bind to three Re atoms in the lattice, leaving under-coordinated active nucleation sites. c) Se atom bonded with the protruding Re atoms to form a stable crystal configuration. d,e) In-plane and cross-section views of Se/ReS_2 heterojunction, where Se atomic chains could grow vertically out of the ReS_2 surface. f,g) The DFT-calculated band structure and DOS spectra for ReS_2 monolayer and Se/ReS_2 heterostructure.

© 2018 WILEY-VCH Verlag GmbH & Co. KGaA, Weinheim

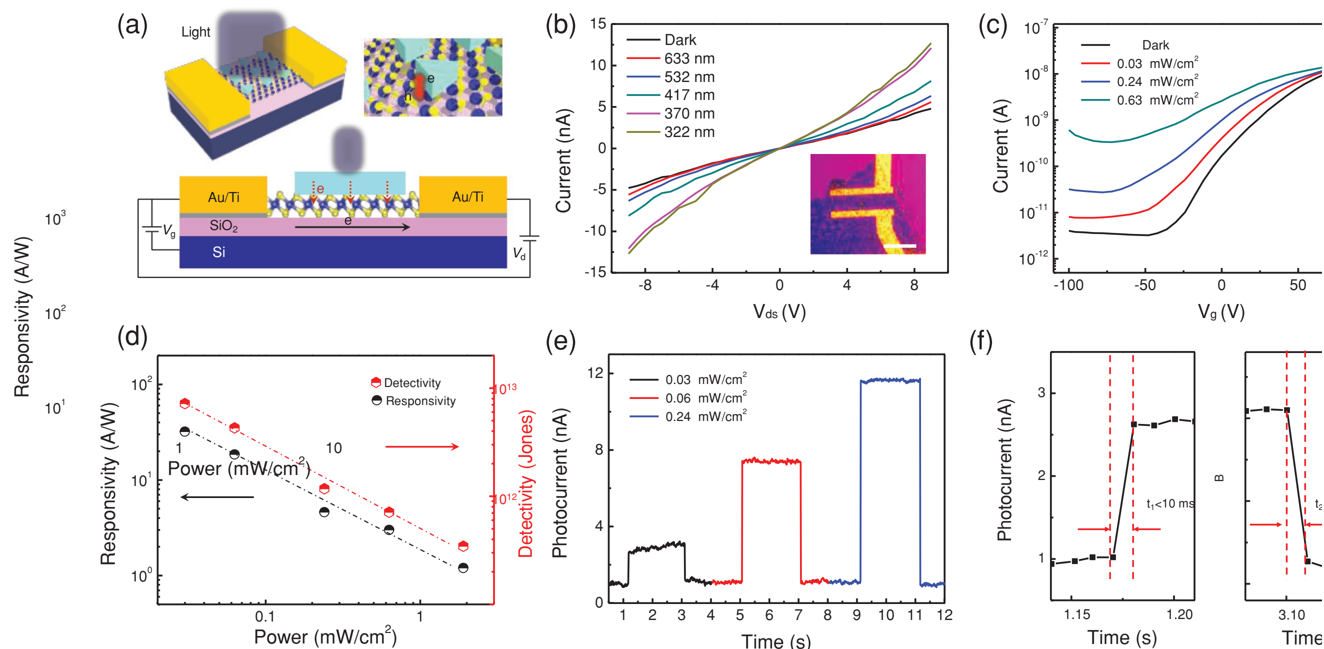

Figure 6. Optoelectronic properties of the Se/ReS_2 heterostructure phototransistor. a) Schematic diagram of a back-gated Se/ReS_2 photodetector. b) Output curves of the device under different illumination wavelengths. Inset shows an optical microscope image of the device, scale bar is 5 µm. c) Transfer curves of the device measured under 370 nm illumination at different power densities at $V_{ds} = 1$ V. d) Plots of R and D^* for different power densities at $V_g = 0$ V. e) Typical rise or decay characteristics of the photocurrent with the laser illumination switched on or off under illumination with different laser power. f) A separated response and reset cycle of the device.

heterostructure. Owing to the suppressed dark current and increased responsivity, detectivity D^* of the hybrid devices could reach up to 8×10^{12} Jones under the same measurement condition, which is almost 3 orders of magnitude larger than that of the monolayer ReS_2 device, and is even superior to that of commercial Si based devices.[46] Both the R_λ and D^* decrease linearly with the incident power, indicating the photoresponse of the hybrid device is mainly determined by the photocarriers.[5] A comparison of the critical parameters between Se/ReS_2 hybrid photodetectors and other analogue hybrid photodetectors is given in the **Table 1**.

Fast response speed is another key factor for high-performance photodetectors, which determines the capability of devices to follow a fast-switching optical signal. Figure 6e shows the comparison of one ON/OFF switching cycle of a Se-ReS_2 device under different incident power densities. The drain current quickly increases up to saturation once the laser is turned on, and it quickly recovers back to original level as the laser is turned off. Both the rise and decay times are less than 10 ms, which is the limit of our measurement set-up (Figure 6f). In contrast, the response speed of ReS_2 photodetectors is much slower, up to 5s. The optoelectronic performance of the devices based on the Se nanobelt-ReS_2 heterostructure was also investigated for comparison. Remarkably, the photoresponse and response speed do not show much difference if no chemical bonding exists at the Se-ReS_2 interface (Figure S14, Supporting Information). These results indicate that the sensitive photoresponse of Se-ReS_2 heterostructure is determined by the chemical hybridization at the material interface.

As mentioned before, the distorted 1T' structure of ReS_2 introduces many intrinsic defects, resulting in significant carrier scattering and slow photocarrier response. In this way, the recombination process of photogenerated electron-hole pairs could be inhibited, resulting in slow response speed.[5,27] In Se-ReS_2 heterostructures, the chemically bonded Se atoms could passivate the defects, and the chemical hybridization at the interface can provide a fast transmission path for photocarrier separation and transfer between Se and ReS_2.[7] Besides,

Table 1. Comparison of critical parameters in various photodetectors.

	Wavelength	Responsivity	I_{ph}/I_{dark}	Response time	Detectivity	Reference
Commercial Si	400 nm				5×10^{12}	[46]
CdS-MoS_3	610 nm	3.91 A W^{-1}		100 ms		[8]
$CH_3NH_3PbI_3$-WS_3	5G5 nm	17 A W^{-1}		7.5 ms	2×10^{12}	[42]
PbSQDs-MoS_2	635 nm	10^5 A W^{-1}		350 ms	10^{11}	[44]
CVD monolayerReS_3	532 nm	13 A W^{-1}		30–50 s		[45]
CdSe/CdS/ZnS QDs-ReS_3	532 nm	604 A W^{-1}		3.2 s		[5]
Exfoliated few-layerReS_3	405 nm	10^4 A W^{-1}	<5	>15 s		[43]
Se-ReS_3	370 nm	36 A W^{-1}	$>10^2$	<10 ms	8×10^{12}	This work

© 2018 WILEY-VCH Verlag GmbH & Co. KGaA, Weinheim

the Se nanocrystals could also act as a recombination center for these photogenerated electron-hole pairs, resulting in reduced composite time once the light is turned off.[8]

3. Conclusion

In conclusion, a new mixed-dimensional heterostructure based on nonlayered Se NPs atop ReS_2 monolayers was achieved using a two-step vapor deposition method. The Se NPs are covalently bonded with the ReS_2 monolayer, exhibiting an epitaxy relationship with the Se (110) plane parallel to the corresponding ReS_2 (010) plane, which was confirmed by XPS, Raman, TEM, and DFT calculations. Owing to the chemical hybridization at the interface, the hybrid Se-ReS_2 photodetectors exhibit a fast response time of less than 10 ms, and detectivity enhanced by almost three orders of magnitude up to 8×10^{12} Jones compared with the monolayer ReS_2 counterpart devices. Overall, our results demonstrated a promising optoelectronic device built on a Se-ReS_2 mixed-dimensional heterostructure, enabling superior device performance beyond traditional TMD-based photodetectors.

4. Experimental Section

Growth of ReS_2 Monolayer: Monolayer ReS_2 was grown by a CVD method in a two-zone furnace. Sulfur powder was placed in the low temperature zone, which was heated to 200 °C at a ramping rate of 5 °C min^{-1} and maintained for 10 min. 20 mg ReO_3 powder (Alfa Aesar, purity: 99.99%) was placed in a ceramic boat in the high-temperature zone with freshly cleaved fluorophlogopite mica above it. The high-temperature zone was heated to 600 °C with a 15 °C min^{-1} ramping rate and maintained for 10 min. Argon with 40 sccm was used as the carrier gas to convey vapor species downstream to the mica substrate.

Raman and STEM Measurements: The synthesized samples were characterized using a HORIBA LabRAM HR800 Raman spectrometer. The system is equipped with a 533 nm wavelength He-Ne excitation laser. Before measurement, the system was calibrated with the Raman peak of Si at 521 cm^{-1}. HAADF-STEM was performed with an FEI Talos F200x with an acceleration voltage of 200 kV.

Device Fabrication and Characterization: The samples were transferred onto 90 nm SiO_2/Si substrates using PMMA-assisted method. EBL was used to pattern electrodes, followed by electron beam evaporation of 30 nm Ti and 100 nm Au as metal contacts. The channel length L_{ch} was designed to be 5 µm while the channel width W_{ch} is 8 µm. The device was measured with a probe station connected to a semiconductor characterization system (4200SCS, Keithley) at room temperature. For photodetection, a laser source (Perot Benchtop) calibrated by a UV-enhanced silicon photodiode was used to provide power-tunable irradiation.

DFT Calculation: DFT calculations were performed with projector augmented-wave pseudopotentials using the Vienna Ab initio Simulation Package. For all DFT calculations, the generalized gradient approximation with the Perdew–Burke–Ernzerhof functional was used. Van der Waals interactions were included using density functional methods optB88. In ionic relaxation calculations, the plane-wave kinetic energy cutoff was 650 eV. The Brillouin zone was sampled with a Gamma cantered mesh of dimensions $8 \times 8 \times 1$ for ReS_2 and $4 \times 4 \times 1$ for structures with S and Se atom absorbed. The convergence criteria for electronic self-consistent loop were set to 1×10^{-6} eV. The optimization persisted until the maximum Hellmann–Feynman force was below 0.01 eV Å^{-1} for all atoms. 16 Å vacuum is used to eliminate interactions between periodic adjacent cells.

Supporting Information

Supporting Information is available from the Wiley Online Library or from the author.

Acknowledgements

J.-K.Q. and G.Q. contributed equally to this work. J.-K.Q. is supported by Chinese Scholarship Council. The work is in part supported by AFOSR/NSF EFRI 2DARE program, ARO and SRC. H.W. and J. J. acknowledge the funding support from the Office of Naval Research (N00014-16-1-2465) and the U.S. National Science Foundation (DMR-1565822) for the TEM/STEM effort. The authors would like to thank Shi-Bin Deng at Purdue university for the discussion of charge transfer mechanism.

P.D.Y. and X.C.Y. conceived the idea and supervised the experiments. J.-K.Q performed the growth experiments and analyzed the experimental data. J.-K.Q. and G.Q. performed device fabrication and analyzed the experimental data. A.R.C. and D.Z. performed and supervised the XPS analysis. W.Z.S. and L.Z. analyzed the growth mechanism. Y.Q.D. performed the SEM measurement. J.J. performed the STEM measurement. H.Y.W. analyzed and supervised STEM experiment. J.-K.Q., G.Q., and P.D.Y. co-wrote the manuscript.

Conflict of Interest

The authors declare no conflict of interest.

Keywords

CVD, epitaxial growth, mixed-dimensional heterostructure, photodetectors, ReS_2 monolayers, Se nanoplates

Received: September 4, 2018
Published online:

[1] Y. Deng, Z. Luo, N. J. Conrad, H. Liu, Y. Gong, S. Najmaei, P. M. Ajayan, J. Lou, X. Xu, P. D. Ye, *ACS Nano*. **2014**, *8*, 8292.
[2] V. Kumaresan, L. Largeau, A. Madouri, F. Glas, H. Zhang, F. Oehler, A. Cavanna, A. Babichev, L. Travers, N. Gogneau, *Nano Lett.* **2016**, *16*, 4895.
[3] Y. Li, J. K. Qin, C. Y. Xu, J. Cao, Z. Y. Sun, L. P. Ma, P. A. Hu, W. Ren, L. Zhen, *Adv. Funct. Mater.* **2016**, *26*, 4319.
[4] Y. Li, C. Y. Xu, J. K. Qin, W. Feng, J. Y. Wang, S. Zhang, L. P. Ma, J. Cao, P. A. Hu, W. Ren, *Adv. Funct. Mater.* **2016**, *26*, 293.
[5] J.-K. Qin, D.-D. Ren, W.-Z. Shao, Y. Li, P. Miao, Z.-Y. Sun, P. Hu, L. Zhen, C.-Y. Xu, *ACS Appl. Mater. Interfaces* **2017**, *9*, 39456.
[6] J.-K. Qin, W.-Z. Shao, C.-Y. Xu, Y. Li, D.-D. Ren, X.-G. Song, L. Zhen, *ACS Appl. Mater. Interfaces* **2017**, *9*, 15583.
[7] Y. Wen, L. Yin, P. He, Z. Wang, X. Zhang, Q. Wang, T. A. Shifa, K. Xu, F. Wang, X. Zhan, *Nano Lett.* **2016**, *16*, 6437.
[8] W. Zheng, W. Feng, X. Zhang, X. Chen, G. Liu, Y. Qiu, T. Hasan, P. Tan, P. A. Hu, *Adv. Funct. Mater.* **2016**, *26*, 2648.
[9] Y. Li, L. Huang, B. Li, X. Wang, Z. Zhou, J. Li, Z. Wei, *ACS Nano* **2016**, *10*, 8938.
[10] D. Kozawa, A. Carvalho, I. Verzhbitskiy, F. Giustiniano, Y. Miyauchi, S. Mouri, A. Castro Neto, K. Matsuda, G. Eda, *Nano Lett.* **2016**, *16*, 4087.
[11] X. Zhu, N. R. Monahan, Z. Gong, H. Zhu, K. W. Williams, C. A. Nelson, *J. Am. Chem. Soc.* **2015**, *137*, 8313.

© 2018 WILEY-VCH Verlag GmbH & Co. KGaA, Weinheim

[12] K. Bogaert, S. Liu, J. Chesin, D. Titow, S. Gradečak, S. Garaj, *Nano Lett.* **2016**, *16*, 5129.
[13] J. A. Miwa, M. Dendzik, S. S. Grønborg, M. Bianchi, J. V. Lauritsen, P. Hofmann, S. Ulstrup, *ACS Nano* **2015**, *9*, 6502.
[14] B. Li, L. Huang, M. Zhong, Y. Li, Y. Wang, J. Li, Z. Wei, *Adv. Electron. Mater.* **2016**, *2*, 1600298.
[15] F. Withers, O. Del Pozo-Zamudio, A. Mishchenko, A. Rooney, A. Gholinia, K. Watanabe, T. Taniguchi, S. Haigh, A. Geim, A. Tartakovskii, *Nat. Mater.* **2015**, *14*, 301.
[16] H. Zhu, J. Wang, Z. Gong, Y. D. Kim, J. Hone, X.-Y. Zhu, *Nano Lett.* **2017**, *17*, 3591.
[17] A. Surrente, D. Dumcenco, Z. Yang, A. Kuc, Y. Jing, T. Heine, Y.-C. Kung, D. K. Maude, A. Kis, P. Plochocka, *Nano Lett.* **2017**, *17*, 4130.
[18] Q. Zheng, W. A. Saidi, Y. Xie, Z. Lan, O. V. Prezhdo, H. Petek, J. Zhao, *Nano Lett.* **2017**, *17*, 6435.
[19] Y. Du, G. Qiu, Y. Wang, M. Si, X. Xu, W. Wu, P. D. Ye, *Nano Lett.* **2017**, *17*, 3965.
[20] J. Qin, G. Qiu, J. Jian, H. Zhou, L. Yang, A. Charnas, D. Y. Zemlyanov, C.-Y. Xu, X. Xu, W. Wu, *ACS Nano.* **2017**, *11*, 10222.
[21] Y. Liu, W. Wu, W. A. Goddard III, *J. Am. Chem. Soc.* **2018**, *140*, 550.
[22] T. I. Lee, S. Lee, E. Lee, S. Sohn, Y. Lee, S. Lee, G. Moon, D. Kim, Y. S. Kim, J. M. Myoung, *Adv. Mater.* **2013**, *25*, 2920.
[23] B. Yu, W. Liu, S. Chen, H. Wang, H. Wang, G. Chen, Z. Ren, *Nano Energy* **2012**, *1*, 472.
[24] L.-B. Luo, X.-B. Yang, F.-X. Liang, J.-S. Jie, Q. Li, Z.-F. Zhu, C.-Y. Wu, Y.-Q. Yu, L. Wang, *CrystEngComm.* **2012**, *14*, 1942.
[25] J.-H. Choi, S.-H. Jhi, *J. Phys.: Condens. Matter* **2018**, *30*, 105403.
[26] P. Miao, J. K. Qin, Y. Shen, H. Su, J. Dai, B. Song, Y. Du, M. Sun, W. Zhang, H. L. Wang, *Small* **2018**. *14*, 1704079.
[27] D. Ghoshal, A. Yoshimura, T. Gupta, A. House, S. Basu, Y. Chen, T. Wang, Y. Yang, W. Shou, J. A. Hachtel, *Adv. Funct. Mater.* **2018**, *28*, 1801286.
[28] M. S. Kim, S. J. Yun, Y. Lee, C. Seo, G. H. Han, K. K. Kim, Y. H. Lee, J. Kim, *ACS Nano* **2016**, *10*, 2399.
[29] F. Federspiel, G. Froehlicher, M. Nasilowski, S. Pedetti, A. Mahmood, B. Doudin, S. Park, J.-O. Lee, D. Halley, B. Dubertret, *Nano Lett.* **2015**, *15*, 1252.
[30] Z. Chen, L. Zhao, K. Park, T. A. Garcia, M. C. Tamargo, L. Krusin-Elbaum, *Nano Lett.* **2015**, *15*, 6365.
[31] N. Kiyofumi, I. Katsunori, M. Yasuhiko, *Jpn. J. Appl. Phys.* **1981**, *20*, 463.
[32] S. Joshi, C. Lokhande, *Appl. Surf. Sci.* **2006**, *252*, 8539.
[33] H. Liu, B. Xu, J.-M. Liu, J. Yin, F. Miao, C.-G. Duan, X. Wan, *Phys. Chem. Chem. Phys.* **2016**, *18*, 14222.
[34] D. H. Kang, M. S. Kim, J. Shim, J. Jeon, H. Y. Park, W. S. Jung, H. Y. Yu, C. H. Pang, S. Lee, J. H. Park, *Adv. Funct. Mater.* **2015**, *25*, 4219.
[35] X. Zhou, Y. Liu, H. Ju, B. Pan, J. Zhu, T. Ding, C. Wang, Q. Yang, *Chem. Mater.* **2016**, *28*, 1838.
[36] M. Shenasa, S. Sainkar, D. Lichtman, *J. Electron Spectrosc. Relat. Phenom.* **1986**, *40*, 329.
[37] H. Cai, E. Soignard, C. Ataca, B. Chen, C. Ko, T. Aoki, A. Pant, X. Meng, S. Yang, J. Grossman, *Adv. Mater.* **2016**, *28*, 7375.
[38] J. Ji, X. Song, J. Liu, Z. Yan, C. Huo, S. Zhang, M. Su, L. Liao, W. Wang, Z. Ni, *Nat. Commun.* **2016**, *7*, 13352.
[39] P. Cherin, P. Unger, *Inorg. Chem.* **1967**, *6*, 1589.
[40] S. Tongay, H. Sahin, C. Ko, A. Luce, W. Fan, K. Liu, J. Zhou, Y.-S. Huang, C.-H. Ho, J. Yan, *Nat. Commun.* **2014**, *5*, 3252.
[41] B. Li, L. Huang, M. Z. Zhong, N. J. Huo, Y. T. Li, S. X. Yang, C. Fan, J. H. Yang, W. P. Hu, Z. M. Wei, J. B. Li, *ACS Nano* **2015**, *9*, 1257.
[42] C. Ma, Y. M. Shi, W. J. Hu, M. H. Chiu, Z. X. Liu, A. Bera, F. Li, H. Wang, L. J. Li, T. Wu, *Adv. Mater.* **2016**, *28*, 3683.
[43] J. Shim, A. Oh, D. H. Kang, S. Oh, S. K. Jang, J. Jeon, M. H. Jeon, M. Kim, C. Choi, J. Lee, *Adv. Mater.* **2016**, *28*, 6985.
[44] D. Kufer, I. Nikitskiy, T. Lasanta, G. Navickaite, F. H. Koppens, G. Konstantatos, *Adv. Mater.* **2015**, *27*, 176.
[45] X. Li, F. Cui, Q. Feng, G. Wang, X. Xu, J. Wu, N. Mao, X. Liang, Z. Zhang, J. Zhang, *Nanoscale* **2016**, *8*, 18956.
[46] X. Gong, M. Tong, Y. Xia, W. Cai, J. S. Moon, Y. Cao, G. Yu, C.-L. Shieh, B. Nilsson, A. J. Heeger, *Science* **2009**, *325*, 1665.

© 2018 WILEY-VCH Verlag GmbH & Co. KGaA, Weinheim